Figures of merit for focusing mega-electron-volt ion beams in biomedical imaging and proton beam writing

Minqin Ren,[a] Harry J. Whitlow,[b] and Ananda Sagari A. R.
Department of Physics, University of Jyväskylä, P.O. Box 35 (YFL), FIN-40014, Finland

Jeroen A. van Kan, Thomas Osipowicz, and Frank Watt
Centre for Ion Beam Applications, Department of Physics, National University of Singapore, 2 Science Drive 3, Singapore 117542, Singapore

(Received 15 June 2007; accepted 28 October 2007; published online 3 January 2008)

A figure of merit (FOM) has been developed for focusing quadrupole multiplet lenses for ion micro- and nanobeam systems. The method which is based on measurement of the central peak of the two-dimensional autocorrelation function of an image provides separate FOM for the horizontal and vertical directions. The approach has been tested by comparison with the edge widths obtained by nonlinear fitting the edge widths of a Ni grid and found to be reliable. The FOM has the important advantage for ion beam imaging of biomedical samples that the fluence needed is considerably lower than for edge fitting. © *2008 American Institute of Physics*. [DOI: 10.1063/1.2827106]

I. INTRODUCTION

Mega-electron-volt (MeV) ion beams focused to nanometer dimensions are emerging as a superior method for direct writing nanometer scale structures in polymers and Si.[1] The vanishingly small proximity exposure,[2–4] capability to directly write high vertical to wall thickness aspect ratio patterns,[5] nanoimprint lithography stamps,[6] nanofluidic devices,[7,8] three-dimensional structures,[5,9,10] tissue growth substrates,[11–13] as well as waveguides[14–17] and porous-Si light emitters.[18,19] The powerful possibilities offered by this rapidly evolving technique have lead to its inclusion in the Japanese Roadmap for Nanoscience.[20]

The physics of the interactions of MeV protons with matter is quite different from 1 to 1000 keV electrons such as used in electron microscopy. This gives focused MeV ion beams [e.g., using the scanning transmission ion microscopy (STIM) technique] the potential for high quality structural imaging of a relatively thick specimens of biological cells and tissue.[21,22]

The best results for focusing proton and He beams with MeV energies to nanometer sized beam spots have been obtained using quadrupole triplet lens systems.[23] These lens systems produce a demagnified image of a precision aperture with different horizontal and vertical demagnifications, D_x and D_y. The quadrupole elements are usually connected so that achieving optimum focus requires simultaneous optimization of two currents. This is in contrast to microscopy and lithography using ultraviolet (UV) photons or electrons where the best focus condition in normal operation only requires optimization of a single parameter. Close to the optimum focus in a quadrupole triplet configuration, the focusing actions in the horizontal and vertical directions are largely decoupled from each other.

Here we present a study on developing a procedure to yield separate figures of merit (FOM) in the horizontal and vertical directions. This procedure, which is based on the two-dimensional (2D) autocorrelation function (ACF),[24] can provide a real time indication of focus quality for manual (and passive automatic) focusing[25] in proton beam lithography and imaging with quadruple multiplet lens systems.

A. Focus figure of merit

For an imaging system, the intensity function $a(x,y)$ of the image is the convolution of the object $O(x,y)$ with the point spread function $P(x,y)$. For an imaging system based on scanning a pointlike probe beam over the object, the point spread function defines how the flux is distributed within the beam spot. Detailed knowledge of the form of $P(x,y)$ is important for image restoration algorithms, e.g., Ref. 26. However, to optimize the image sharpness it is sufficient to parameterize only the spreading of $P(x,y)$ which is a minimum at optimum focus. In the case of quadrupole multiplets $P(x,y)$ is not rotationally invariant because of difference in D_x and D_y and separate focusing powers in the horizontal and vertical directions.

Figures of merit must satisfy a number of criteria. The most important being that they are reproducible and have well defined extreme values that define the minimum widths of $P(x,y)$ without local extrema that destroy monotonic behavior around the optimum.[27,28] Moreover, it is desirable that the figures of merit use information from the entire 2D field so that the fluence on any spot in the field of view is uniform and small. This is particularly important for biological samples where high beam fluences lead to significant shrinkage[29] or where a fiducial mark is used for focusing in proton beam writing (PBW) with fluences below the exposure threshold for the resist or creating porous Si.[9,19] Other criteria include that the figure of merit should be insensitive to the form and orientation of the sample and should only be sensitive to the information contained in the image, rugged

[a]Present address: Centre for Ion Beam Applications, Department of Physics, National University of Singapore, 2 Science Drive 3, Singapore 117542, Singapore.
[b]Electronic mail: harry_j.whitlow@phys.jyu.fi.

in that it is insensitive to noise and edge response and no additional operator interaction in the form of adjustable parameters should be needed.

The insensitivity to detail of the edge response is particularly important when secondary electrons are used to form the image because the yield is enhanced in the vicinity of edges.[25] The noise immunity is also an important aspect for figure of merit ruggedness because images in proton beam writing and MeV ion microscopy usually exhibit significant counting statistical variations associated with the low brightness of the current accelerator ion sources. The situation is further accentuated by the need to determine separate horizontal and vertical figures of merit.

Rossi *et al.*[30] have proposed a method for determining the width of a rotationally invariant point spread function for an ion microbeam, e.g,[31] by using a Fourier optics approach to derive the parameter from measurements of the modulation transfer function (MTF). The method is not well suited to the determination of focus figures of merit for quadrupole multiplet lenses because it requires some modification to handle the requirement of rotational invariance (discussed earlier) and also requires collection of separate images from suitable grids with different spatial frequency patterns. Furthermore, if ion-induced secondary electron images are used, the yield enhancement at the edge[25] implies that the MTF cannot be obtained from the contrast transfer function[30] by a straightforward bar transformation, e.g., Refs. 32–34.

One widely used approach to tune the beam focus is to make horizontal and vertical line scans over sharp horizontal and vertical edges (e.g., a test grid) while monitoring a suitable signal and optimize the edge sharpness either by ocular inspection or by nonlinear fitting of a suitable function.[25] The signals can be the energy loss of transmitted ions, off-axis forward scattered ions, or the secondary electron yield. Although this procedure generally works well, and can be automated,[25] the high fluences of ions which impinge on the small number of pixels along these lines the grid may lead to changes in the edge and focal plane positions through localized buildup of contamination, swelling, and thermal distortion of the grid. Mechanical alignment of the focusing sample is also an important issue with this method. The focusing sample requires alignment of the grid bar edges along the horizontal and vertical directions and also the focal plane must be transferable within the depth of field to other samples.

A number of other approaches have been applied for autofocusing in microscopy that include optimizing the average 2D gradient,[27,28,35,36] frequency domain filtering,[27,28,36,37] direct optimization of the mean variance,[28,36–38] maximum contrast,[36] and extracting sharpness information from the ACF.[27,36] The ACF approach exhibits a high ruggedness against statistical noise[27,36] and for this reason extraction of a sharpness parameter from the ACF was chosen as the basis for the FOM. This was selected in preference to the variance method because of the well-known tendency of the regions with few counts to contribute more to the variance as compared to the edge and central regions with better counting statistics. Similarly, because the high frequency sharpness and noise components are overlapped in the frequency domain and spread out which makes it not straightforward to maximize the sharpness components in the spatial frequency distributions. A further advantage of the ACF is that it is completely defined from a single image. This avoids uncertainties associated with variations in edge positions and depth of field variations when moving between different samples or areas on the same sample.

B. The autocorrelation function

For a 2D image with the intensity function $a(x,y)$ the ACF is

$$r(\acute{x},\acute{y}) = \int_{-\infty}^{\infty}\int_{-\infty}^{\infty} a(\acute{x},\acute{y})a(\acute{x}-x,\acute{y}-y)dxdy. \tag{1}$$

Rather than calculating the 2D ACF directly it is faster to calculate from the power spectrum $P(u,v)=|G(ju,jv)|^2$ using the Wiener–Khinchin relationship[39]

$$r(\acute{x},\acute{y}) = \frac{1}{4\pi^2}\int_{-\infty}^{\infty}\int_{-\infty}^{\infty} P(u,v)e^{-j(u\acute{x}+v\acute{y})}dudv, \tag{2}$$

where $G(ju,jv)$ is the Fourier transform of the intensity function

$$G(ju,jv) = \int_{-\infty}^{\infty}\int_{-\infty}^{\infty} a(x,y)e^{-j(uv+vy)}dxdy. \tag{3}$$

When the 2D ACF is transformed by swapping quadrants so that $(\acute{x},\acute{y})=(0,0)$ is located at the center of the ACF, it has the useful property that the sharpness information about $P(x,y)$ from the entire brightness function is mapped into the central peak. The shape of the central ACF peak along the $\acute{x}$ and $\acute{y}$ directions from Eq. (1) is uniquely determined by the shape of the point spread function, $P(x,y)$, in the horizontal and vertical directions. This integration of sharpness information from the whole image, as will be seen later, allows a straightforward suppression of pixel to pixel counting statistical variation.

II. EXPERIMENTAL

The proton beam writing facility at the National University of Singapore was used for the tests. A proton beam was obtained from a 3.5 MV Singletron accelerator coupled to a 90° magnetic dipole sector operated in slit stabilization mode. After passing through the object aperture the beam was steered by a switching magnet into a 6.3 m drift length before entering the lithography end station that consisted of a Oxford Microbeams magnetic beam scanner, followed by a quadrupole triplet with 70 mm working distance to the sample mounted on a computer controlled precision *X-Y-Z* stage.[40] The proton induced secondary electron yield was used to image the sample which consisted of a Ni focusing grid.

The focusing grid used for this work was fabricated by writing the pattern by PBW and subsequently electrodepositing Ni in a plating bath before detachment and resist stripping.[23] A special feature of this grid is that the bars are

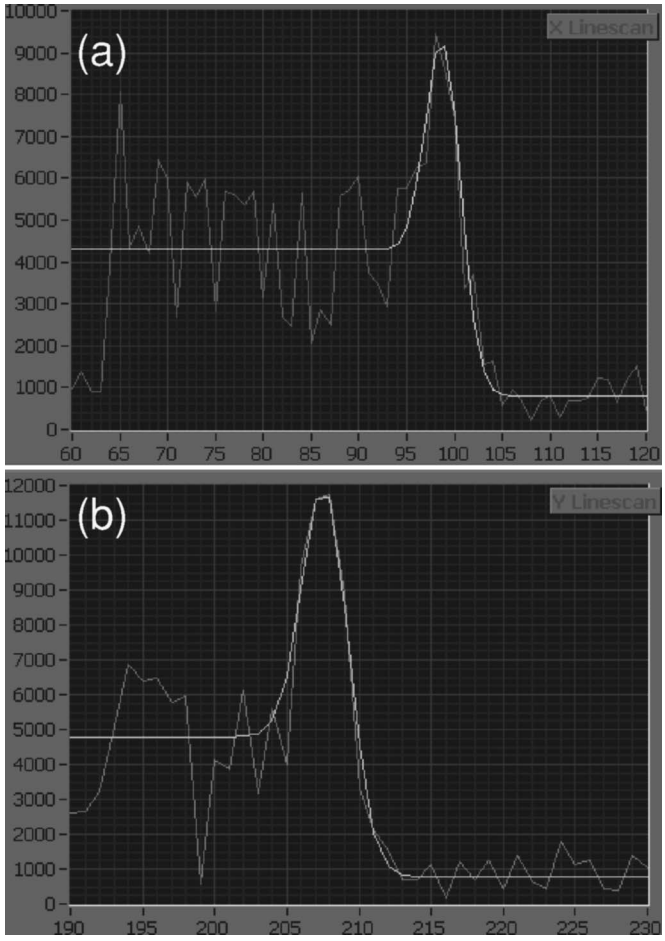

FIG. 1. (a) Horizontal and (b) vertical line scans over the focus grid bar edges.

not orthogonal. The angle between the horizontal and vertical bars was determined by optical microscopy to be $84.0° \pm 0.4°$.

Coarse focusing was carried out by ocular inspection of the beam spot fluorescence on a quartz target. Subsequently, in order to obtain a focus condition very close to the optimal, the edge sharpness was monitored as the beam was scanned in a line across the grid bar edges in the horizontal and vertical directions. Figure 1 illustrates the secondary electron yield for the line scans at the focus. The peaks at the edges are associated with the enhanced secondary electron yield at the slit edges. Subsequently, a series of images was acquired where the horizontal and vertical lens currents were varied in steps through focus. The ACF $r(\acute{x},\acute{y})$ was calculated from bitmap images of $a(x,y)$ from Eqs. (2) and (3) using the FFTPACK5 software package.[41]

Investigations of the feasibility of directly focusing on biological cells were carried out using the direct STIM technique[21] with 1 MeV $^4He^+$ ions. The in-focus spot size was determined from measurements on the grid bar to be 100×110 nm. MCF-7 breast cancer cells (American Type Culture Collection) were directly cultured on the SiO_2 surface of the Si positive-intrinsic-negative detector following the preparation protocol which is given in Rf. [21]

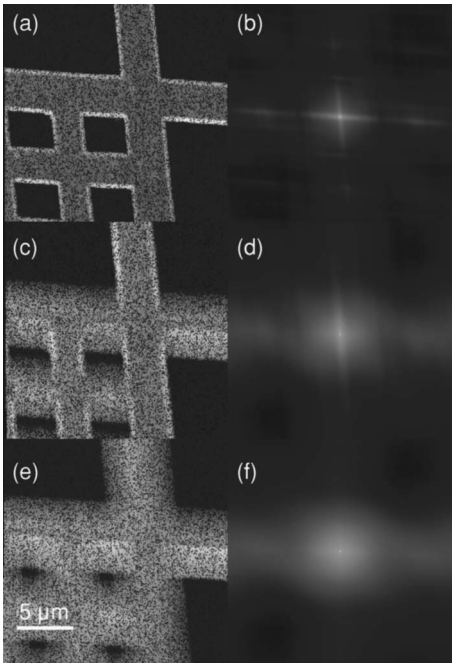

FIG. 2. Grey scale representation of secondary electron image [(a), (c), (e)] and corresponding 2D ACF [(b), (d), (f)] for different focus conditions [(a) and (b)] optimal focus, [(c) and (d)] vertical focus—12 steps from optimal, [(e) and (f)] horizontal and vertical—24 and—12 steps from optimal.

III. RESULTS AND DISCUSSION

Figure 2 presents examples of the in-focus and out-of-focus grid images and the associated ACF where both the horizontal and vertical lens currents were stepped and when only the horizontal lens current is out of focus. The effect defocusing on the ACF may be directly observed. We consider first the in-focus case, Figs. 2(a) and 2(b). The ACF shows a central peak with a very intense point at the center which is associated with the pixel to pixel counting statistical. The horizontal and vertical components can be readily distinguished as well as the structure away from the central peak that is associated with the grid periodicity. Note also that the grid image angular orientation information is preserved in the ACF. The angles between the grid bars is $80.6° \pm 0.6°$ corresponding to an additional skew of $3.4° \pm 0.7°$ that is probably associated with the high scan rates used to acquire the images causing lag in the magnetic raster deflection system. Figure 3 presents cuts along the ACF in the horizontal and vertical directions for the case where the horizontal lens excitation was a maintained constant while the focus was stepped through focus in the vertical direction. Counting statistical variations are uncorrelated from one pixel to another and therefore give rise to a contribution only in a single pixel located at the center of the 2D ACF. In subsequent parameterization of the FOM the high frequency pixel-to-pixel counting statistical noise was be suppressed by neglecting the contribution from this pixel.

Inspection of the data in Fig. 3 shows that the width of the central part of the ACF in the vertical direction [Fig. 3(b)] is strongly influenced by the vertical excitation current, while for the horizontal direction [Fig. 3(a)] although the amplitude changes, the width and shape remain quite similar.

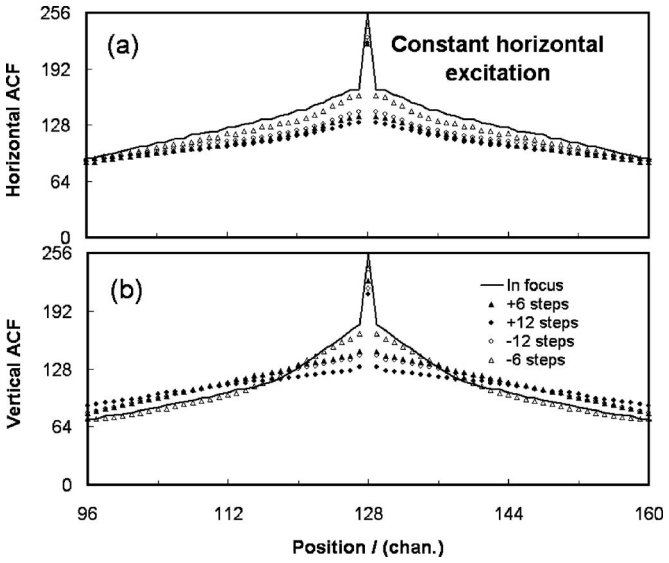

FIG. 3. Area-normalized horizontal (a) and vertical (b) cuts through the ACF in the region of the central peak as the vertical lens excitation was stepped through the focus while the horizontal maintained a constant for the sample shown in Fig. 2.

This defocusing in the vertical direction can be clearly seen by comparing Figs. 2(a), 2(c), and 2(b), 2(d). The figures of merit in the horizontal and vertical directions were taken to be the root-mean-square (rms) widths, $\sigma_x = \langle \Delta X^2 \rangle^{1/2}$ and $\sigma_y = \langle \Delta Y^2 \rangle^{1/2}$. To optimize the sensitivity of σ_x and σ_y to the contribution to the central peak associated with focus sharpness, the figure of merit calculation included only pixels which exceeded 85% of the maximum value. This choice of the threshold value was found by a cut and try approach to be noncritical and provide good immunity to secondary peaks associated with periodic structure in the sample.

To test the performance of the figures of merit for focusing, σ_x and σ_y were compared with edge widths obtained by nonlinear fitting of an edge function[25] to line scans across the grid bar edges. The edge function was taken to be a rectangle convoluted with a Gaussian summed with a Gaussian that modeled the enhanced secondary electron emission for sharp edges. (Fig. 1) The two Gaussians were assumed to have the same full width half maximum (FWHM). Figure 4 compares the edge width obtained from nonlinear fitting with the figures of merit figure from the ACF. In this figure it is clearly seen that the horizontal and vertical minimum widths [Figs. 4(a) and 4(c)] obtained from nonlinear fitting and the figures of merit σ_x and σ_y [Figs. 4(b) and 4(d)] have minimum at the focus. As expected when the excitation in both directions is stepped through the focus the widths and figures of merit in the horizontal and vertical directions show the same behavior with a minimum value at optimum. Repeated measurements at the optimum point also exhibit small variations in the values. These variations are generally small compared to the variations associated with defocusing and might arise from the precision of the magnet currents, magnetic hysteresis effects, and also possibly changes in the focusing grid due to heating and deposition of contamination. A further observa-

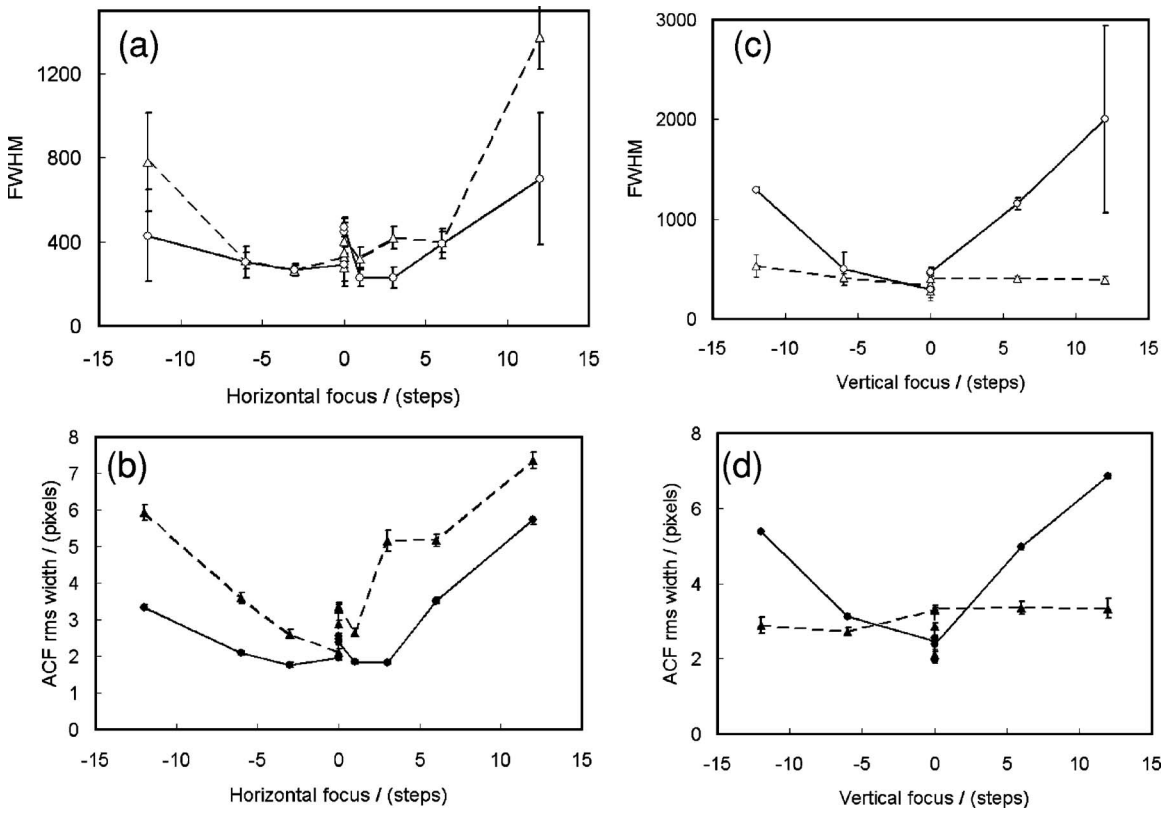

FIG. 4. Comparison as the lens excitation currents are scanned through focus of nonlinear fitting widths [(a), (c)] with figures of merit [(b), (d)] σ_x and σ_y. In (a) and (b) both the horizontal and vertical excitations are varied. In (c) and (d) the vertical excitation is stepped through the focus while the horizontal excitation maintained at focus. The triangles and dashed lines refer to the horizontal parameters while the circles and full line denotes the parameters in the vertical direction. The error bars represent the statistical uncertainty in calculating the fitted width and σ_x and σ_y.

tion that can be made from Fig. 4 is that as the focus in the vertical direction is changed sσ_x [Figs. 4(c) and 4(d)] remains essentially constant while the fitted vertical width and σ_y increases as the beam is stepped towards under and over focus. This behavior is less pronounced when defocusing takes place in the horizontal direction (not shown) although again here both the figures of merit and fitted widths show the same trend.

The error bars in Fig. 4 associated with the statistical uncertainties are smaller for the figures of merit σ_x and σ_y than the nonlinear fitting. The larger error bars from nonlinear fitting are particularly significant under conditions of strong defocusing. This is strong but not conclusive evidence that the figures of merit are a more reliable measure of focus quality under strong defocusing conditions. This is presumably a consequence of the fact that, as noted earlier, σ_x and σ_y are determined from the whole of the image field, whereas in the nonlinear fitting the counting statistical errors are larger because of the restriction in fluence imposed since only a small fraction of the pixels in the field are irradiated in line scans. The implication of this is that the ACF approach will be more tolerant of low fluences where the variations in counting statistics are more significant. This will allow the possibility of directly focusing on the sample while introducing a minimum of beam-induced changes. This is extremely important for focusing on individual biological cells, as discussed later, which are extremely labile.

The faithful reproduction of the optimum focus conditions and the lower sensitivity to counting statistical uncertainties indicate that the figures of merit σ_x and σ_y derived from the 2D ACF may be used with confidence for focusing MeV ion beams using quadrupole multiplet lenses to nanometer dimensions.

The speed of computation of the FOM is of importance for both manual and automatic focusing. For the 256×256 pixel images used in this study the time taken to calculate the 2D ACF and σ_x and σ_y and write bitmap files takes $\sim$0.5 s on a personal computer with an Intel 2 GHz T2500 processor. This is much faster than the time taken to scan an image and sufficiently fast for the FOM to be used as a real-time focus monitor or as a signal for autofocusing.

For focusing in nuclear microscopy using labile biological samples, a fluence as low as possible must be used to minimize the risk of shrinkage.[29] Figure 5 shows in and out of focus images obtained using the NanoSTIM technique[21] under low- and high-fluence conditions. In the images the intensity scale represents the mean energy loss. In Figs. 5(b) and 5(d) the gray scale of the 2D ACF has been normalized using the ImageJ software[42] so only the central peak region between 80% and 100% of maximum intensity is shown. The σ_x and σ_y values for the in-focus and off-focus conditions were $9.3\pm0.7, 8.0\pm0.7$ and $11.5\pm0.7, 12.6\pm0.8$ pixel widths, respectively. From Figs. 5(a) and 5(c) it can be clearly seen that in the low fluence case the statistical noise in the image does not allow the degree of focus to be discerned by eye, the width of the central peak in the ACF is still a meaningful measure of focus. It should be kept in mind that for objects that are not orthogonal, such as a cell or circular aperture, the defocusing in one direction also introduces image spreading in the perpendicular direction which is also seen in the ACF. Colocalization of the low- and high-fluence images was investigated by merging images with different color channels to test for shrinkage of the cell. No evidence of ion induced shrinkage was seen even when comparing a series of high-fluence images. This would show up as characteristic bands of color around features such as edges. The noise immunity of the ACF as a focusing FOM allows its use in direct STIM to focus on individual cells of interest without introducing significant shrinkage.

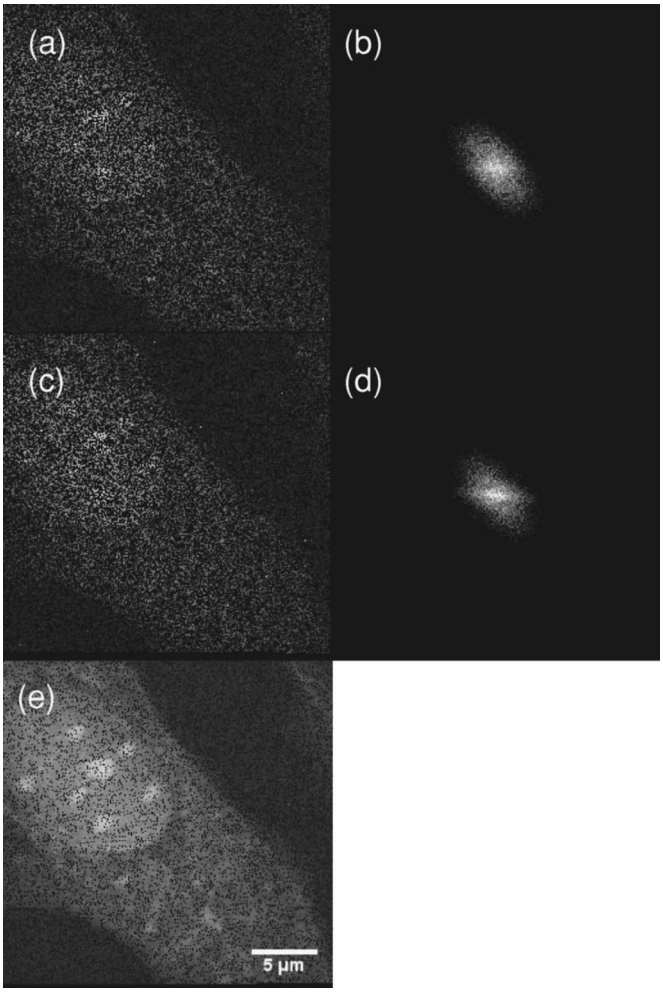

FIG. 5. Direct STIM images (Ref. 21) of a human breast cancer cell and corresponding ACF. (a) and (b) are off-focus measured under low-fluence conditions (3.6×10^4 ions corresponding to 5.8×10^9 ions cm^{-2}). (c) and (d) correspond to in-focus under low-fluence conditions and (e) corresponds to in-focus under high-fluence conditions (3.2×10^5 ions corresponding to 1.4×10^{11} ions cm^{-2}). In (b) and (d) the gray scale has been optimized to show the central peak region only.

IV. CONCLUSIONS

A rugged method to obtain figures of merit for MeV ion beams focused using quadrupole multiplet lenses to nanometer dimensions for proton beam writing and imaging has been developed and tested. The approach is based on the characterization of the central peak in the 2D autocorrelation function in terms of the rms widths in orthogonal directions. The method allows simple filtering to minimize the effects of pixel to pixel statistical noise and makes no assumption as

the structure of the sample. The rms widths of the ACF correctly reproduced the optimum focus condition and the behavior under defocusing conditions of the FWHM beam profile that was determined from the same data by nonlinear fitting. Evaluation of the figure of merit takes ~0.5 s using a modern processor which is sufficiently fast to allow the figures of merit to be used for manual focusing and automatic focus control. The noise immunity of the ACF allows its use for directly focusing on individual cells of interest without introducing detectable beam induced shrinkage.

ACKNOWLEDGMENTS

This work has been supported by the Academy of Finland Centre of Excellence in Nuclear and Accelerator-Based Physics (Ref. 213503). H.J.W. is also grateful to the Magnus Ehrnrooth's Foundation for travel support that made this study possible. We are most grateful to Lim Daina, Chan Yee Gek, and Professor Bay Boon Huat of the Department of Anatomy at the National University of Singapore, who prepared the sample used for the STIM study.

[1]F. Watt, A. A. Bettiol, J. A. van Kan, E. J. Teo, and M. B. H. Breese, Int. J. Nanosci. **4**, 269 (2005).
[2]J. A. van Kan, A. A. Bettiol, and F. Watt, Nano Lett. **6**, 579 (2006).
[3]H. J. Whitlow, M. L. Auželité, I. A. Maximov, J. A. van Kan, A. Bettiol, and F. Watt, Nanotechnology **15**, 223 (2004).
[4]C. N. B. Udalagama, A. A. Bettiol, and F. Watt, Nucl. Instrum. Methods Phys. Res. B **260**, 390 (2007).
[5]K. Ansari, J. A. van Kan, A. A. Bettiol, and F. Watt, Appl. Phys. Lett. **85**, 476 (2004).
[6]J. A. van Kan, A. A. Bettiol, and F. Watt, J. Micromech. Microeng. **16**, 1967 (2006).
[7]K. A. Mahabadi, I. Rodriguez, S. C. Haur, J. A. van Kan, A. A. Bettiol, and F. Watt, J. Micromech. Microeng. **16**, 1170 (2006).
[8]P. G. Shao, J. A. Van Kan, L. P. Wang, K. Ansari, A. A. Bettol, and F. Watt, Appl. Phys. Lett. **88**, 093515 (2006).
[9]E. J. Teo, M. B. H. Breese, E. P. Tavernier, A. A. Bettiol, F. Watt, M. H. Liu, and D. J. Blackwood, Appl. Phys. Lett. **84**, 3202 (2004).
[10]J. A. van Kan, A. A. Bettiol, and F. Watt, Appl. Phys. Lett. **83**, 1629 (2003).
[11]J. L. Sanchez, G. Guy, J. A. van Kan, T. Osipowicz, and F. Watt, Nucl. Instrum. Methods Phys. Res. B **158**, 185 (1999).
[12]F. Sun, D. Casse, J. A. Van Kan, R. Ge, and F. Watt, Tissue Eng. **10**, 267 (2004).
[13]S. Gorelick, P. Rahkila A. Sagari A. R., T. Sajavaara, S. Cheng, L. B. Karlsson, J. A. van Kan, and H. J. Whitlow, Nucl. Instrum. Methods Phys. Res. B **260**, 130 (2007).
[14]A. A. Bettiol, T. C. Sum, J. A. van Kan, and F. Watt, Nucl. Instrum. Methods Phys. Res. B **210**, 250 (2003).
[15]T. C. Sum, A. A. Bettiol, S. Venugopal Rao, J. A. van Kan, A. Ramam, and F. Watt, Proc. SPIE **5347**, 160 (2004).
[16]A. A. Bettiol, S. Venugopal Rao, E. J. Teo, J. A. van Kan, and F. Watt, Appl. Phys. Lett. **88**, 171106 (2006).
[17]T. C. Sum, A. A. Bettiol, C. Florea, and F. Watt, J. Lightwave Technol. **24**, 3803 (2006).
[18]E. J. Teo, M. B. H. Breese, A. A. Bettiol, D. Mangaiyarkarasi, F. Champeauz, F. Watt, and D. Blackwood, Adv. Mater. **18**, 51 (2006).
[19]D. Mangaiyarkarasi, E. J. Teo, M. B. H. Breese, A. A. Bettiol, and D. J. Blackwood, J. Electrochem. Soc. **152**, D173 (2005).
[20]The New Energy and Industrial Technology Development Organization (NEDO), Japan, Roadmap for Nanofabrication (May 2007), http://www.nedo.go.jp/roadmap/, pp. 65–69 (in Japanese).
[21]M. Ren, J. A. van Kan, A. A. Bettiol, D. Lim, Y. G. Chan, B. H. Bay, H. J. Whitlow, T. Osipowicz, and F. Watt, Nucl. Instrum. Methods Phys. Res. B **260**, 124 (2007).
[22]H. J. Whitlow, M. Ren, J. A. van Kan, F. Watt, and D. White, Nucl. Instrum. Methods Phys. Res. B **260**, 28 (2007).
[23]J. A. van Kan, P. G. Shao, P. Molter, M. Saumer, A. A. Bettiol, T. Osipowicz, and F. Watt, Nucl. Instrum. Methods Phys. Res. B **231**, 170 (2005).
[24]P. A. Lynn, *An Introduction to the Analysis and Processing of Signals* (Macmillan, London, 1973), p. 85.
[25]C. N. B. Udalagama, A. A. Bettiol, J. A. van Kan, E. J. Teo, M. B. H. Breese, T. Osipowicz, and F. Watt, Nucl. Instrum. Methods Phys. Res. B **231**, 389 (2005).
[26]D. S. C. Biggs and M. Andrews, Appl. Opt. **36**, 1766 (1997).
[27]C. F. Batten, "Autofocusing and Astigmatism Correction in the Scanning Electron Microscope," Master's thesis, University of Cambridge, 2000; www.mit.edu/cbatten/work/sem-mphil00.pdf.
[28]F. C. Groen, I. T. Young, and G. Liqthart, Cytometry **6**, 81 (1985).
[29]F. Watt, P. S. P. Thong, A. H. M. Tan, and S. M. Tang, Nucl. Instrum. Methods Phys. Res. B **130**, 188 (1997).
[30]P. Rossi, D. K. Brice, and B. L. Doyle, Nucl. Instrum. Methods Phys. Res. B **210**, 85 (2003).
[31]P. Rossi, B. L. Doyle, V. Auzelyte, F. D. McDaniel, and M. Mellon, Nucl. Instrum. Methods Phys. Res. B **249**, 242 (2006).
[32]R. L. Lucke, Appl. Opt. **37**, 7248 (1998).
[33]I. Kandarakis, D. Cavouras, N. Kalivas, C. D. Nomicos, and G. S. Panayiotakis, Nucl. Instrum. Methods Phys. Res. B **155**, 199 (1999).
[34]J. W. Coltman, J. Opt. Soc. Am. **44**, 468 (1954).
[35]J. M. Geusebroek, F. Cornelissen, A. W. Smeulders, and H. Geerts, Cytometry **39**, 1 (2000).
[36]A. Santos, C. Ortiz de Solórzano, J. M. Peña, N. Malpica, and F. Del Pozo, J. Microsc. **188**, 264 (1997).
[37]L. Firestone, K. Cook, K. Culp, N. Talsania, and K. Preston, Jr., Cytometry **12**, 195 (1991).
[38]G. P. Allen, R. M. Hodgson, S. R. Marsland, G. Arnold, R. C. Flemmer, J. Flenley, and D. W. Fountain, Twenty-First International Conference, Image and Vision Computing, (IVCNZ), New Zealand, 2006.
[39]N. G. van Kampen, *Stochatic Processes in Physics and Chemistry* (North Holland, Amsterdam, 1981), p. 61.
[40]F. Watt, J. A. Van Kan, I. Rajta, A. A. Bettiol, T. F. Choo, M. B. H. Breese, and T. Osipowicz, Nucl. Instrum. Methods Phys. Res. B **210**, 14 (2003).
[41]J. Burkart, Fortran90 FTPACK5 fast Fourier transform (2007); http://people.scs.fsu.edu/~burkardt/f_src/fftpack5/ffpack5.html.
[42]W. S. Rasband and J. Image, Image processing and analysis in JAVA, U. S. National Institutes of Health, Bethesda, MD, http://rsb.info.nih.gov/ij/index.html, 1997–2006.